Running title: Modelling ECM dysfunction in haemorrhagic stroke

Adult organotypic brain slice cultures recapitulate extracellular matrix remodelling in haemorrhagic stroke

Benjamin J. Hewitt, PhD [1] – b.hewitt@bham.ac.uk
Lauren Roberts, BSc [2] **-** 129088318@aston.ac.uk
James A. Roberts, PhD [1] **–** j.roberts.6@bham.ac.uk
Daniel Fulton, PhD [3,4] **-** d.fulton@bham.ac.uk
Lisa J. Hill, PhD [1] - l.j.hill@bham.ac.uk
Phillip Kitchen, PhD [2] – p.kitchen1@aston.ac.uk
Roslyn M. Bill, PhD [2] – r.m.bill@aston.ac.uk
Hannah F. Botfield, PhD [3,4] – h.botfield@bham.ac.uk

[1] Department of Biomedical Sciences, School of Infection, Inflammation and Immunology, College of Medicine and Health, University of Birmingham, Birmingham, UK.

[2] Aston Institute for Membrane Excellence, Aston University, Birmingham, UK

[3] Inflammation and Ageing, School of Infection, Inflammation and Immunology, College of Medicine and Health, University of Birmingham, Birmingham, UK.

[4] Birmingham Centre for Neurogenetics, University of Birmingham, Birmingham, UK.

Corresponding authors:

Dr Benjamin Hewitt, PhD - Mailing address: Neuroscience and Ophthalmology, Robert Aitken Institute for Clinical Research, University of Birmingham, Birmingham, B15 2PA, United Kingdom. Tel: +44(0)121 414 8859

Dr Hannah Botfield, PhD - Mailing address: Neuroscience and Ophthalmology, Robert Aitken Institute for Clinical Research, University of Birmingham, Birmingham, B15 2PA, United Kingdom.

Running title: Modelling ECM dysfunction in haemorrhagic stroke

1. Abstract

Haemorrhagic stroke is a devastating condition characterised by vessel rupture and free blood within the brain parenchyma or cerebrospinal fluid (CSF) filled spaces. Across the major subtypes of haemorrhagic stroke (subarachnoid, intracerebral, and intraventricular haemorrhages), the presence of blood in the CSF generates significant tissue damage in the first 72 hours after the event, known as early brain injury (EBI). EBI includes neuroinflammation, blood-brain barrier breakdown and dysregulation of extracellular matrix (ECM) dynamics. ECM dysfunction has been shown to trigger fibrosis of the cortical blood vessels, limiting normal CSF circulation and resulting in the buildup of metabolic waste or the development of post-haemorrhagic hydrocephalus. Limiting or preventing this fibrosis may therefore reduce the rate of morbidity experienced by survivors, providing a potential avenue for non-surgical treatment to reduce secondary brain injury post-stroke.

Despite this, current *in vivo* approaches fail to differentiate between the effect of blood products and secondary consequences including intracranial pressure (ICP) elevation and mass effect. Here, we describe an adult rat organotypic brain slice culture (OBSC) model of haemorrhagic stroke which enables the identification of the effect of blood products on ECM dysregulation. We demonstrate the distribution of key cell types across a time course of 0, 3 and 7 days in culture, indicating that such cultures are viable for a minimum of 7 days. Using immunofluorescence staining, Western blotting and RNA sequencing, we show that exposure of OBSCs to lysed blood markedly increases ECM deposition around cortical blood vessels. This is accompanied by dysregulation of ECM regulatory genes and upregulation of inflammation and oxidative stress-related genes, successfully recapitulating the changes seen in human stroke survivors. This versatile *ex vivo* model provides a translational platform to further understanding of haemorrhagic stroke pathophysiology and develop or trial novel therapeutics prior to progression to *in vivo* stroke studies.

2. Introduction

Haemorrhagic stroke is a devastating condition characterised by vessel rupture and free blood within the brain parenchyma or cerebrospinal fluid (CSF)-filled spaces, and may be split into intracerebral haemorrhage, subarachnoid haemorrhage (SAH) and intraventricular haemorrhage depending on the location of the bleed. While haemorrhagic stroke only accounts for approximately 20% of stroke cases [1], the risk of mortality or profound disability is markedly greater than that posed by ischemic stroke [2].

SAH is most commonly triggered by a ruptured aneurysm causing blood to leak into the CSF in the subarachnoid space, with blood also entering the ventricles in higher grade SAH. Early brain injury (EBI) is the injury that occurs in the brain within 72 hours of an SAH and develops due to mechanical factors and the direct effect of free blood. SAH causes an increase in intracranial pressure (ICP), decreased cerebral blood flow (resulting in global ischemia), blood brain barrier (BBB) breakdown, brain oedema, oxidative stress and neuroinflammation, which ultimately leads to neurodegeneration [3].

Extracellular matrix (ECM) dynamics in and around the brain are also affected following SAH. There is a fine balance between ECM deposition and degradation which is particularly evident within blood vessel architecture. Under pathological conditions, BBB dysfunction is associated with the degradation of ECM in the basement membrane, mainly through matrix metalloproteinases. This can then release growth factors such as the pleiotropic cytokine transforming growth factor-β1 (TGF-β1) which in turn stimulates vascular smooth muscle cells (SMCs) to promote ECM deposition and repair the BBB [4]. SAH can result in excessive or dysregulated ECM deposition around major blood vessels on the surface of the brain, contributing to the development of cerebral vasospasm and subsequent delayed cerebral ischemia [4]. Furthermore, elevated TGF-β1 levels have been implicated in the development of subarachnoid fibrosis and ECM dysfunction in CSF drainage pathways after SAH which can

lead to the development of post-haemorrhagic hydrocephalus [5–8]. Understanding the pathways and mechanisms involved in ECM dysfunction may provide therapeutic targets for reducing further brain injury following SAH.

In both human patients and animal models of SAH, it can be difficult to differentiate between the response of the brain to the mechanical factors that follow a stroke (ICP elevation, mass effect) and the direct reaction of brain tissue to blood products, which is important to understand the pathogenesis of common sequalae to SAH and focus the development of future therapeutics to treat these. In contrast, *ex vivo* models allow us to differentiate between these factors to identity and further understand disease processes. Organotypic brain slices cultures (OBSCs), which were first described in the 1950s for the study of membrane potentials in the cerebral cortex [9], have been used in the study of neurodegenerative diseases [10], invasive glioma [11] and epilepsy [12] amongst many other uses. OBSCs provide a three-dimensional tissue architecture and are widely considered to be more representative of the *in vivo* state than cell cultures due to the presence of neurons, glial cells and endothelial cells in a native tissue architecture [13]. OBSCs are typically prepared from neonatal brain tissues slices as these tend to be more resistant to the mechanical trauma caused by sectioning, making them easier to culture [14]. However, these neonatal models are unlikely to recapitulate the complexity or maturity of adult tissues, as is shown by different responses to sectioning. For this reason, adult OBSC models are essential in modelling a disease which primarily affects middle to older-aged adults [15]. Whilst adult rodent OBSCs are now well established, there has been very limited prior exploration of their application to haemorrhagic stroke research. Attempts at short-term (minutes to hours) haemorrhagic stroke brain slice models have been reported with a focus on neuronal survival, though it is not clear whether they were from adult or neonatal animals [16]. Therefore, the development and validation of an adult OBSC system capable of modelling haemorrhagic stroke remains an important challenge.

Here, we describe the generation and validation of OBSCs derived from healthy adult rats and their application to the *ex vivo* modelling of post-haemorrhagic stroke ECM dysfunction and inflammation. *Ex vivo* recapitulation of ECM dynamics may provide an opportunity for furthering understanding of the molecular mechanisms underlying this key factor in post-stroke brain injury and offer a platform in which to trial novel therapeutics prior to use *in vivo*.

108 # 3. Methods

109 ## 3.1. Tissue culture

110 All tissue culture was performed under aseptic conditions using a class II microbiological
111 safety cabinet (Monmouth Guardian T1200). Tissues were cultured at 37°C, 5% CO_2 and
112 100% relative humidity.

113 Dissection media for OBSC generation comprised Earle's balanced salt solution
114 supplemented to a final concentration of 25 mM HEPES. OBSC culture media comprised 1:1
115 Dulbecco's Modified Eagle Media (DMEM):Neurobasal A, supplemented with final
116 concentrations of 2% (v/v) B-27, 2 mM L-glutamine and 1% penicillin/streptomycin solution.

117 ## 3.2. Experimental animals

118 Male Sprague-Dawley rats were group housed with access to food and water *ad libitum*, on a
119 12-hour light/dark cycle. All studies were conducted at the University of Birmingham, and
120 both the establishment and investigators held relevant UK Home Office licenses. Animals
121 were monitored daily and group housed, with no regulated procedures performed. Animals
122 were euthanized according to Schedule 1 of the Animals (Scientific Procedures) Act 1986 at a
123 weight of 130-150 g by intraperitoneal injection of 200 mg/ml pentobarbitol, 4 ml/kg and
124 decapitated following cessation of circulation. Blood was captured in a sterile, un-heparinised
125 50 ml centrifuge tube and stored at -20°C until required.

126 ## 3.3. Organotypic brain slice culture (OBSC) generation

127 The brain was rapidly removed from the skull and the cerebellum and olfactory bulbs excised
128 with a sterile scalpel. A flat face was produced on the rostral and caudal edges of the brain by
129 cutting (Figure 1), and the brain adhered to the chuck of a vibratome (7000smz, Campden

130 Instruments) (caudal side down) with cyanoacrylate glue. The brain was then mounted into
131 the vibratome bath, containing 250 ml dissection medium on ice, bubbled with medical
132 oxygen at 2 psi. 250 µM sections were produced with the vibratome set to a 1.25 mm
133 amplitude at 80 Hz and sections stored in the dissection media bath until completion.

134

135 Slices were then transferred to 6-well polyethylene culture inserts (657641, Greiner) using a
136 fine paintbrush and spatula. To facilitate this, 1 ml of culture medium was initially added to
137 each insert to enable floating of the slice, which was removed once the slice was correctly
138 positioned. Culture inserts were added to a standard 6-well plate (3516, Corning), and 1.5 ml
139 of OBSC culture medium added to the bottom well with the top insert containing the brain
140 slice left dry. Slices were then either fixed immediately or on day in-vitro (DIV) 3 or 7 using
141 4% paraformaldehyde (PFA) in PBS for one hour at room temperature, followed by two, one-
142 hour phosphate buffered saline (PBS) washes at room temperature prior to storage in PBS at
143 4°C.

144 **3.4. <u>Blood-treated OBSCs</u>**

145 OBSCs destined for blood treatment as a model of haemorrhagic stroke were generated as
146 described above and exposed to blood immediately or after 7 days of pre-culture.

147 Blood from all animals was pooled, vortexed and shaken vigorously to break up clots, and
148 diluted 1:1 with PBS. 6, 24 or 48 hours prior to the experiment endpoint, 175 µl of diluted
149 blood (or PBS control) was added to the wells assigned for blood treatment after removal of
150 an equal volume of medium. Brain slices for immunohistochemical analysis were then fixed
151 as previously described, prior to washing through two changes of PBS and storage at 4°C.

152 Slices destined for protein or RNA extraction were dissected under a surgical microscope,
153 with the cortex removed (taking care to avoid capturing any tissue from the corpus callosum),
154 snap frozen in liquid nitrogen and stored at -80°C.

155 **3.5. Immunohistochemical staining and imaging**

156 OBSCs were divided into two hemispheres prior to staining. A full protocol for staining and
157 clearing of OSBCs can be found in the supplemental materials ('Staining and clearing of
158 OBSCs'). Antibodies were diluted in PBS with 0.2% (v/v) triton X-100, 6% (v/v) goat serum
159 and 20% (v/v) DMSO, with 0.2 ml of diluted antibody added to each slice in a 24-well plate.
160 Imaging was performed using an AxioScan Z.1 (Zeiss) for blood exposed sections and an
161 AxioScan 7 (Zeiss) for timepoint studies maintaining the same imaging settings across all
162 slides within an analysis group. 4,6-diamidino-2-phenylindole (DAPI) was included at a
163 1:5000 dilution of a 5 mg/ml stock in PBS.

164

165 **3.6. Image processing and analysis**

166 Image processing was performed using FIJI [17], with the operator blinded to the treatment or
167 culture conditions of each image by displaying only numerical filenames. Representative
168 images shown have been enhanced for display by modification of window and level,
169 performed uniformly across all images within a comparison group or stain. No image
170 enhancement was performed on images prior to image analysis.

171 Images were processed using a FIJI macro [17], made available both on GitHub
172 (https://github.com/Dr-ben-hewitt/OBSC-quantification-macros) and in the supplementary
173 materials. In brief, this performed a maximum intensity projection and presented the user
174 with an image in the red channel only (corresponding to blood vessel staining with RECA-1).

175 Five regions of interest (ROIs) were then manually selected in the cortex of each slice and
176 processed for background subtraction (100 pixel radius for RECA-1 channel, 1000 pixel
177 radius for fibronectin and collagen IV), followed by automatic thresholding of blood vessels
178 (RenyiEntropy method) and ECM proteins (Triangle method), with image calculation then
179 performed to find the average of these two sets of features.

180 Mean pixel intensity per unit area was calculated by user selection of 3 ROIs per image (with
181 the user shown only the DAPI channel to limit bias), followed by background subtraction (50
182 pixel radius) in FIJI, automated measurement of the integrated ROI pixel intensity and
183 division of this value by the area of the ROI.

184 **3.7. <u>Protein extraction and Western blotting</u>**

185 Protein extraction was performed by mechanical homogenisation in 250 µl
186 radioimmunoprecipitation assay (RIPA) buffer, supplemented with protease and phosphatase
187 inhibitors per manufacturers guidance. Samples were then incubated on a roller at 4°C for 2
188 hours and centrifuged at 10,000×*g* for 20 minutes at 4°C. Supernatant was then harvested,
189 aliquoted and stored at -80°C until required. Protein concentration was assessed by BCA
190 assay, following the manufacturer's instructions. SDS-PAGE was performed using 2.5 µg of
191 protein in a 20 µl volume, containing 5 µl LDS sample buffer and 2 µl reducing agent, on 4-
192 12% bis-tris polyacrylamide gels using MOPS-SDS running buffer. Electrophoresis was
193 performed at 120 V for 90 minutes. Proteins were then transferred to a nitrocellulose
194 membrane using NuPAGE transfer buffer at 25 V for 1 hour. Blocking was performed by
195 immersion in 5% (w/v) skimmed milk in tris-buffered saline with 0.1% (v/v) Tween-20
196 (TBST) for one hour at room temperature. Blots were then incubated in primary antibodies
197 for fibronectin or collagen IV and alpha-actin diluted in blocking buffer for one hour at room
198 temperature, washed three times in TBST (15 minutes each, room temperature), and

199 incubated in secondary antibody (1:5000 anti-IgG HRP conjugated) for one hour at room
200 temperature. Blots were then washed 3x in TBST (10 minutes each, room temperature) prior
201 to immersion in chemiluminescent substrate for 5 minutes (room temperature) and imaging
202 (G:Box chemi XRQ, Syngene).

203 **3.8. RNA extraction, sequencing and RT-qPCR**

204 Samples were mechanically disrupted and homogenised in 1 ml TRIzol and 200 µl
205 chloroform was then added. Samples were then mixed by shaking and centrifuged at
206 12,000*g* for 15 minutes at 4°C. The upper aqueous phase was removed and transferred to a
207 new tube, and an equal volume of molecular grade 70% ethanol added. RNA was then
208 extracted from the sample with an RNEasy mini extraction kit (Qiagen), following the
209 manufacturer's instructions for a 40 µl elution volume in RNase free water. RNA was then
210 quantified by spectrophotometery (N50 NanoPhotometer, Implen). Sample quality control
211 (integrity, purity and concentration via Agilent 5400) and paired-end mRNA sequencing was
212 performed by a contracted 3rd party (Novogene, UK) using a NovaSeq X Plus (Illumina) at a
213 read depth of 20 million reads per sample.

214 Alignment against a Sprague Dawley rat genome (rn_celera) was performed by Novogene,
215 followed by mapping to the same reference genome using the featureCounts tool [18] on the
216 Galaxy platform [19], followed by quality control using MultiQC [20]. Analysis of differentially
217 expressed genes was performed with DESeq2 [21], with comparisons made of expression in
218 blood-treated samples against an untreated control. Differentially expressed genes were
219 defined as those with an adjusted p-value (*pAdj)* < 0.05, and a fold change cutoff of 2 was
220 used for display of DEGs.

221 Gene ontology (GO) analysis was performed on all differentially expressed genes (with no
222 fold-change cutoff) using goseq [22], with gene categories retrieved from the rn6 assembly due

223 to unavailability of gene categories for the rn_celera assembly. All visualisation of RNA-
224 sequencing data was performed using GraphPad Prism 10.3.

225 Validation of the top 6 most upregulated and top 6 most downregulated genes was performed
226 using RT-qPCR. In brief, cDNA conversion was performed with a Tetro cDNA kit using
227 Oligo(dT)18 primers and 100 ng of RNA. cDNA was then further diluted by addition of 20 µl
228 molecular biology grade water. RT-qPCR mastermix comprised 100 µl SYBR green, 78 µl
229 water and 1 µl of each forward and reverse primer (reconstituted to 100 µM). 9 µl mastermix
230 was added to each well of a 384-well PCR plate, followed by 1 µl cDNA. RT-qPCR was
231 performed using a QuantStudio 5, with reaction conditions shown in supplemental materials
232 **Error! Reference source not found.**1. Oligonucleotide primers used are shown in
233 supplemental materials Table S2

234

235 **3.9. <u>Statistical analysis</u>**

236 All statistical analysis was performed in GraphPad Prism 10.3, with a significance level of
237 0.05. Statistical tests are described in the relevant figure legends.

238 RT-qPCR data were analysed with QBase+ (Biogazelle, Belgium) using the calibrated
239 normalised relative quantity (CNRQ) method. Four housekeeping genes were assessed using
240 the geNorm algorithm within QBase+ and the two housekeeping genes with lowest mean
241 variability were used as reference genes for sample normalisation.

242 **3.10. <u>Key resources table</u>**

243 Table 2.

244 # 4. Results

245 ## 4.1. Health of the OBSCs after 7 days in culture

246 Cleaved caspase-3 (CPP3) staining was used as a marker of apoptosis. Overall, there was an
247 increase in CCP3-positive staining from DIV0 to DIV7 in the cortex (Figure 2A) and other
248 areas of the OBSC (Figure S3). Quantification of the mean CCP3-positive pixel intensity per
249 unit area revealed a significant increase in CCP3 signal in the cortex (Figure 2B), increasing
250 from 1.21×10^{-6} at 0 days to 2.04×10^{-6} at 3 days ($P = 0.0081$) and 2.72×10^{-6} at 7 days ($P =$
251 0.0001). A significant increase in CCP3 signal between DIV0 and DIV7 was also noted in the
252 basal ganglia (Figure S3).

253 ## 4.2. Alterations in the organotypic cytoarchitecture of the cortex after 7 days in culture

254 Previous studies suggested OBSCs need to be cultured for 7-14 days prior to use in order to
255 allow the slices to recover from the trauma of vibratome sectioning. Therefore, the cellular
256 composition of OBSCs was assessed at DIV0, DIV3 and DIV7.

257 NeuN, a neuronal cell marker, demonstrated stable levels in the cortex of OBSCs at DIV0,
258 DIV3 and DIV7 (Figure 3A), with no significant differences observed in NeuN staining
259 intensity between DIV0 (mean pixel intensity per unit area of $1.21\text{x}10^{-5}$) and DIV3 or 7
260 ($8.49\text{x}10^{-6}$ and $6.24\text{x}10^{-6}$ respectively, Figure 3B). In the cortex, glial fibrillary acidic protein
261 (GFAP)-positive astrocytes (Figure 3C) appeared to show a marked reduction in staining
262 from DIV0 to DIV7, particularly with a loss in the glia limitans. This was further supported
263 by a significant reduction in quantified GFAP mean pixel value at both DIV3 and DIV7
264 compared to DIV0. Mean pixel intensity per area of GFAP was reduced by more than 50%
265 from 5.3×10^{-6} at DIV0 to 2.0×10^{-6} and 2.5×10^{-6} at DIV3 and DIV7 ($P < 0.0001$ and $P =$

266 0.0001, respectively) (Figure 3D). In contrast, GFAP-positive astrocytes were maintained
267 within the deeper subcortical white matter (supplemental materials, Figure S4).

268

269 Ionized calcium-binding adapter molecule 1 (IBA1) was used as a microglial cell marker.
270 There was a reduction in IBA1-positive cells in the cortex in DIV3 and DIV7 compared to
271 DIV0 (Figure **4**A). Image analysis showed a significant reduction after 3 and 7 days of
272 culture, from a mean IBA1 pixel intensity per unit area of 4.87×10^{-6} at DIV0 to 1.69×10^{-6} at
273 DIV3 and 1.63×10^{-6} at DIV7 (Figure **4**B, $P = 0.0150$ and 0.0134 respectively). However,
274 similar to GFAP staining, there did not appear to be any significant changes in IBA1 staining
275 in the subcortical white matter (Figure S4).

276

277 Alpha-smooth muscle actin (αSMA) labels vascular smooth muscle cells present within
278 arteries, arterioles and pericytes. In contrast to the other cell markers, αSMA-positive staining
279 (Figure **5**A) increased along blood vessel structures in the cortex between DIV0 and DIV3
280 and DIV7. Image analysis revealed a significant increase in αSMA mean pixel value per unit
281 area from 1.1×10^{-6} at DIV0 to 2.4×10^{-6} at DIV7 ($P = 0.0061$) (Figure **5**B). Finally, rat
282 endothelial cell antigen 1 (RECA-1) staining, which recognizes a cell surface antigen on
283 endothelial cells, showed a reduction in staining of small vessels and capillaries at DIV3 and
284 7 (Figure **5**C). Image analysis (Figure **5**D) showed a marked and significant reduction in
285 mean RECA-1 pixel value per unit area in the cortex, falling from 5.4×10^{-6} at DIV0 to
286 1.9×10^{-6} and 1.8×10^{-6} at DIV3 and DIV7 respectively ($P = 0.0003$ for both). A similar
287 outcome was shown in the deeper tissues in proximity to the basal ganglia (Figure S4).

288

289

290 **4.3. <u>Blood exposure induced increases in fibronectin and collagen deposits in OBSCs</u>**

291 OBSCs were exposed to lysed blood for 6, 24 or 48 hours to mimic haemorrhagic stroke,
292 initiated at either DIV0 (acute) or DIV7 (7-day preculture). Fibronectin staining was shown
293 to be minimal in acute sections (Figure 6A), with image analysis in the cortex and subcortical
294 white matter (Figure 6B and Figure S8, respectively), and Western blotting of cortical protein
295 isolates (Figure 6C and D) showing no significant increase in fibronectin staining or
296 expression at any timepoint ($P > 0.05$ for all). However, control OBSCs cultured for 7 days
297 showed visually greater fibronectin staining (Figure 6E) compared to acute sections (Figure
298 6A). Exposure of these pre-cultured OBSCs to blood resulted in a significant, near 10-fold
299 increase in cortical vessels co-locating with fibronectin, from a mean of 2.97% in control
300 OBSCs to a mean of 28.61% following blood exposure for 48 hours ($P = 0.0123$) (Figure
301 6F). This was further evidenced by a significant increase in fibronectin protein expression as
302 assessed by Western blot, increasing 2.27-fold following blood exposure ($P = 0.038$) (Figure
303 6G and H). No significant change was noted in fibronectin staining in the subcortical white
304 matter (Figure S8).

305 A similar outcome was noted in the staining and expression of collagen IV, with acute OBSCs
306 showing a significant increase in cortical vessel coverage from 1.55% in control samples to
307 16.15% after 24 hours of blood exposure ($P = 0.0491$, Figure 7B). No significant difference
308 was seen in collagen IV staining in the white matter ($P > 0.05$ for all, Figure S8). In contrast
309 to acute cultures, OBSCs treated with blood at DIV7 generated a marked increase in collagen
310 IV signal, increasing from 7.92% cortical vessel coverage by collagen IV in the control to
311 32.84% after blood exposure ($P = 0.0032$, Figure 7D).

312

313 **4.4. RNA-sequencing of blood-exposed OBSCs**

314 Following sample quality control and principal component analysis (supplementary materials
315 Figure S1 and S2), one blood-treated sample (B1) was excluded due to sequencing of an
316 insufficient sample quality leading to poor mapping to the reference genome. All subsequent
317 analysis was performed without this sample. Volcano plots were generated for all
318 differentially expressed genes (DEGs) ($pAdj < 0.05$) with expression fold changes (FC) > 2, (
319 Figure **8**A) and greater than 1.5 (Figure **8**B), with 95 and 604 DEGs over this FC cutoff,
320 respectively. Heatmaps were also generated for each sample across the 25 most upregulated
321 and 25 most downregulated DEGs (Figure **8**C).

322

323 RT-qPCR validation of the top 6 most upregulated and downregulated genes (Figure **9**)
324 showed a significant decrease in *Aspn*, *Epyc*, *H19*, *Mmp8* and *Prss35* transcript expression
325 after blood exposure ($P = 0.0107$, 0.0159, 0.0027, 0.026 and 0.0297 respectively. There was
326 no significant reduction in *Cilp* expression, likely due to high inter-sample variability ($P =$
327 0.2207). Inversely, a significant upregulation of *Il11*, *Ptges* and *Saal1* was shown ($P =$
328 <0.0001, 0.0015 and 0.0006 respectively). Increases in *Kng1*, *Il17rb* and *Tacr* were not
329 significant ($P = 0.1307$, 0.1109 and 0.0667). Overall, 8 of the 12 tested genes showed a
330 significant change in expression (66.7%), with all showing a trend in the same direction as
331 RNA-sequencing data following blood exposure.

332

333 Gene ontology (GO) analysis was then performed across cellular component (CC), biological
334 process (BP) and molecular function (MF) GO families. Within the CC family (Figure **10**A),
335 'extracellular region' and 'extracellular matrix' were the top two most over-represented GO
336 terms (gene ratios 0.137 and 0.285, *padj* 6.45×10^{-29} and 8.96×10^{-27} respectively). DEGs from

extracellular region (Figure **10**B) and extracellular matrix terms (Figure **10**C) showed downregulation in blood-treated OBSCs including *Col11a1*, *Col4a6* and *Eln*, downregulation of *Mmp8* and upregulation of *Mmp9*, *Mmp3* and *Timp1*.

'Response to external stimulus' and 'response to chemical' were the top two most over-represented terms within the BP family (Figure **10**D). 'Inflammatory response' and 'response to oxidative stress' were selected for display (gene ratios 0.141 and 0.149, *padj* 9.64×10^{-11} and 1.06×10^{-7} respectively), with DEGs from these terms shown in Figure **10**E and F respectively. Blood exposure appeared to cause a marked upregulation of included cytokines and cytokine receptors, including *Ccl20*, *Il1rn*, *Il1r1* and *Il17rb*.

In the MF family, 'glycosaminoglycan binding' and 'signalling receptor binding' were the topmost over-represented terms (Figure **10**G). 'Signalling receptor binding' and 'cytokine activity' were selected for display (gene ratios 0.129 and 0.168, *padj* 6.55×10^{-10} and 5.85×10^{-5}), with DEGs from these terms shown in Figure **10**H and Figure 10I, respectively. Blood exposure led to an increase in expression of *Il11*, *Csf3*, *Fgf7* and *Lbp* and a downregulation in *Igf2* and *Fbln5*, as examples.

356 ## 5. Discussion

357 We have described an approach to the generation of adult rat OBSCs and their novel
358 application to the development of an *ex vivo* haemorrhagic stroke model. We demonstrate that
359 blood products have direct effects on ECM regulation in cortical blood vessels at both the
360 transcript and protein level. In addition, we have characterised the distribution and number of
361 several key brain cell types (neurons, endothelial cells, arterial smooth muscle/pericytes,
362 astrocytes and microglia) after 0, 3 and 7 days in culture. All cell types were present across
363 the measured time-course but showed differences in their response to culture conditions.

364 No significant change was noted in NeuN-positive cell staining, suggesting neurons were not
365 substantially impacted by the length of time in culture. In contrast, there was a significant
366 reduction in cortical GFAP-positive cells, particularly in the glia limitans, observed between
367 DIV0 and DIV3/7. This could be due to either loss of astrocytes or reduction in GFAP
368 expression within astrocytes. The latter seems plausible as the mechanical injury caused by
369 vibratome sectioning has been shown to cause glial cell activation, a hallmark of which is
370 GFAP upregulation [23,24]. The reduction in GFAP levels observed in our study could therefore
371 represent the return of GFAP to resting levels following an initial slicing-induced spike [25].
372 Quantification of astrocyte number is required to confirm this idea, but if correct, this
373 interpretation would support the rationale for culturing brain slices for longer periods of time
374 [13] before initiating studies in these models. Interestingly, GFAP levels were not reduced
375 everywhere in the brain slice, and GFAP-positive staining was maintained over the time-
376 course within the subcortical white matter. IBA1-positive microglia in the cortex also reduced
377 from DIV0 to DIV3/7. Delbridge *et al*., reported a reduction in microglial proliferation and
378 an increase in microglial inflammation in the days following slice preparation [26], likely
379 leading to the observed fall in microglia numbers seen here.

380 We did observe a significant reduction in RECA-1 staining, particularly associated with
381 capillaries, suggesting a loss of endothelial cells (ECs) from the OBSCs. We suggest that the
382 lack of blood flow, and thus the lack of a pulsatile hemodynamic force and shear stress
383 experienced by the ECs [27], contributes to this loss. Previous studies have shown that
384 decreased blood flow directly affects EC migration and cytoskeleton reorganisation [28], and
385 causes apoptosis and a reduction in EC number in previously dilated arteries [29]. Alternatively,
386 our data could be explained by a reduction in the abundance of the RECA-1 epitope (an
387 unknown protein) within endothelial cells which has been suggested by Moser and colleagues
388 [30]. At the same time, an increase in αSMA-positive cells was seen at DIV 7, suggesting a rise
389 in the number of arterial smooth muscle cells (SMCs) or pericytes. Previous studies show a
390 causative link between reduced blood flow and disordered vascular remodelling [31] and
391 increased SMC proliferation (shown initially in hypertensive models) [32].

392 CCP3 staining increased between DIV0 and DIV3/7, indicating an increase in apoptosis-
393 driven cell death, which is to be expected due to the acclimatisation of slices to culture
394 following the injurious process of vibratome sectioning. This finding does suggest a possible
395 upper limit to the culture period, though longer culture durations were not tested in the
396 present work. Overall, these data suggest the successful maintenance of most tested cell types
397 in OBSCs, with a possible degradation in blood vessel endothelium due to a lack of blood
398 flow through the vasculature. For this reason, future works employing this model (for
399 example, studies of the blood brain barrier) may choose to employ a shorter pre-culture
400 period, with the caveat of increased astrogliosis and inflammation.
401 Following this, adult rat OBSCs were cultured for 0 and 7 days and then exposed to lysed rat
402 blood for 6, 24 or 48 hours to mimic haemorrhagic stroke. Two key markers of fibrosis,
403 fibronectin [33,34] and collagen IV [35,36],were both significantly elevated along cortical blood
404 vessels (as measured by immunostaining) only in the 7-day cultures. 48 hours of blood

405 exposure generated the largest response, both on immunofluorescent stains and Western blots.
406 Our results show that these fibrotic deposits are primarily localised to penetrating cortical
407 vessels, where αSMA is most prominent. Interestingly, these deposits were not observed in
408 the 0-day cultures where there were lower levels of αSMA. This potentially indicating the
409 involvement of SMCs or pericytes in modulating ECM associated with blood vessels. The
410 location of ECM deposits suggest they could contribute to disordered glymphatic flow,
411 reducing the clearance of metabolites (and blood products following haemorrhagic stroke)
412 and exacerbating brain injury. Indeed, perivascular fibrosis has previously been reported in
413 *in vivo* models of ICH [37,38] and SAH [39] and directly linked to reduced clearance of amyloid-β
414 after ischemic stroke [40].

415 In addition to immunostaining and Western blotting, RNA sequencing was performed on
416 RNA isolated from 7-day precultured OBSCs exposed to blood for 48 hours. Blood exposure
417 led to significant over-expression of inflammatory response and cytokine signalling related
418 GO terms, driven by a marked upregulation of inflammation-linked genes, including *Ccl20*,
419 *Il11* and *Csf3*. *Ccl20* has previously been linked to neuroinflammation following traumatic
420 brain injury [41] with antagonism shown to reduce this following SAH [42]. *Il11* concentration in
421 plasma post-ICH has been shown to positively correlate with increased mortality and the
422 development of hydrocephalus [43]. *Il11* has also been linked to inflammatory immune cell
423 migration in multiple sclerosis [44] and protection against ischemia reperfusion injury in middle
424 cerebral artery occlusion (MCAO) models of ischemic stroke [45]. *Csf3* has been suggested to
425 play a role in post-MCAO brain injury by increasing neutrophil toxicity [46]. This large drive
426 towards a pro-inflammatory transcriptome following blood exposure supports studies
427 examining the pro-inflammatory nature of blood and blood products in the subarachnoid
428 space and parenchyma following haemorrhagic stroke [47,48] and suggests that this crucial
429 element is successfully recapitulated in our OBSC-based haemorrhagic stroke model.

Interestingly, the same RNA sequencing data showed a downregulation of ECM-related GO terms and genes (including collagens and elastin), with some upregulation of matrix metalloproteinases (MMPs) and tissue inhibitors of metalloproteinases (TIMPs). Immunofluorescent staining and Western blotting of blood-exposed OBSCs suggested a marked increase in ECM deposition along cortical vessels, as previously discussed, suggesting a differential response at the gene and protein level. We propose this increase in protein deposition may not be due to changes in *de novo* protein synthesis, but a manipulation of ECM turnover triggered by blood-induced changes in the expression of MMPs and TIMPs. Indeed, modified *Mmp9*/*Timp1* expression (as shown in our RNA sequencing data) has been linked to disordered collagen deposition in the skin [49] and lung [50]. In the brain, a reduction in collagen IV RNA and upregulation of *Mmp9* has previously been reported 48 hours after SAH [51], a finding reflected in the present work. These findings suggest that our model also successfully mimics the ECM dysfunction seen in haemorrhagic stroke, with a likely breakdown of the blood brain barrier and disordered, fibrotic ECM deposition along cortical penetrating vessels.

A limitation of our model is that it simulates global blood exposure instead of localised blood exposure to the cortical tissues or ventricles (as may be seen after SAH or IVH). Further work may be undertaken to identify if this model can recapitulate the differences seen between types of haemorrhagic stroke, i.e SAH and ICH [8]. Single cell RNA sequencing may also determine which cells drive fibrosis following blood exposure, as the mechanism underlying this has not been explored in the present work.

Our findings suggest that our OBSC model can a) successfully maintain adult rat brain slices for at least 7 days and b) employ lysed blood to recapitulate the disordered ECM deposition (fibrosis) and neuroinflammation which follows haemorrhagic stroke. Future studies may employ this model to further understand the molecular drivers of post-stroke inflammation

455 and fibrosis, or to trial anti-fibrotic agents to reduce ECM dysfunction. Our model offers a
456 platform to advance the translation of pharmacological treatments aimed at reducing post-
457 stroke disability and improving outcomes for stroke survivors, whilst providing a higher
458 throughput and physiologically realistic alternative to *in vivo* animal studies.

459 6. Declarations

460 6.1. Disclosures

461 PK and RMB are founders and shareholders in Estuar Pharmaceuticals. The other authors
462 declare they have no financial and/or non-financial interests that may cause a conflict of
463 interest.

464 6.2. Funding

465 This research was funded by a Medical Research Foundation grant (MRF-076-0002-RG-
466 BOTF-C0754). LR was supported by a Midlands Integrative Biosciences Training
467 Programme studentship (MIBTP, reference BB/T00746X/1) from the Biotechnology and
468 Biological Sciences Research Council (BBSRC). PK is supported by a BBSRC Discovery
469 Fellowship (BB/W00934X/1). RMB is supported by a UKRI Frontier Research Grant
470 EP/Y023684/1 (following assessment as an ERC Advanced grant, FORTIFY, ERC-2022-
471 ADG-101096882 under the UK Government Guarantee scheme) and acknowledges a
472 Biotechnology and Biological Sciences Research Council Pioneer Award (BB/Y512874/1).

473 6.3. Data availability

474 RNA sequencing data have been uploaded to the NCBI sequence read archive (SRA) and are
475 freely available for use (BioProject ID PRJNA1262501). Uncropped, unedited Western blots
476 are included in the supplemental materials (Figures S3 and S4). Image quantification macros

are available (supplemental materials, 'ImageJ macro language scripts used for image quantification'). All other data will be made available upon request to the corresponding authors.

6.4. Authors' contributions (CRediT)

BJH: methodology, software, formal analysis, resources, investigation, data curation, writing – original draft, visualisation. LR: investigation, data curation, writing – review and editing. JAR: formal analysis, writing – review and editing. DF: resources, writing – review and editing. PK: supervision, writing – review and editing. RMB: supervision, writing – review and editing. LJH: supervision, writing – review and editing. HB: resources, writing – review and editing, supervision, project administration, funding acquisition.

7. Acknowledgements

The authors thank the members of the Neuro-Ocular Inflammation and Matrix Research Group (University of Birmingham) for their support and University of Birmingham Biomedical Services Unit staff for their expert assistance in caring for the experimental animals. We acknowledge the support of the Microscopy Technology Hub Facilities at the College of Medicine and Health, University of Birmingham, for providing access to equipment and technical expertise and the Birmingham Environment for Academic Research (BEAR) advanced research computing team for use of high-performance computing services and storage.

The Galaxy server used for some calculations is partly funded by the German Federal Ministry of Education and Research BMBF grant 031 A538A de.NBI-RBC and the Ministry of Science, Research and the Arts Baden-Württemberg (MWK) within the framework of

LIBIS/de.NBI Freiburg. The Aston Institute for Membrane Excellence (AIME) is funded by UKRI's Research England as part of their Expanding Excellence in England (E3) fund.

8. References

1. Donkor ES. Stroke in the 21st Century: A Snapshot of the Burden, Epidemiology, and Quality of Life. *Stroke Res Treat*. 2018;2018:1–10.

2. Waziry R, Heshmatollah A, Bos D, Chibnik LB, Ikram MA, Hofman A, Ikram MK. Time Trends in Survival Following First Hemorrhagic or Ischemic Stroke Between 1991 and 2015 in the Rotterdam Study. *Stroke*. 2020;51:824–829.

3. Lauzier DC, Jayaraman K, Yuan JY, Diwan D, Vellimana AK, Osbun JW, Chatterjee AR, Athiraman U, Dhar R, Zipfel GJ. Early Brain Injury After Subarachnoid Hemorrhage: Incidence and Mechanisms. *Stroke*. 2023;54:1426–1440.

4. Hu Z, Deng X, Zhou S, Zhou C, Shen M, Gao X, Huang Y. Pathogenic mechanisms and therapeutic implications of extracellular matrix remodelling in cerebral vasospasm. *Fluids Barriers CNS*. 2023;20. doi:10.1186/S12987-023-00483-8,.

5. Douglas MR, Daniel M, Lagord C, Akinwunmi J, Jackowski A, Cooper C, Berry M, Logan A. High CSF transforming growth factor β levels after subarachnoid haemorrhage: association with chronic communicating hydrocephalus. *J Neurol Neurosurg Psychiatry*. 2009;80:545–550.

6. Chen S, Luo J, Reis C, Manaenko A, Zhang J. Hydrocephalus after Subarachnoid Hemorrhage: Pathophysiology, Diagnosis, and Treatment. *Biomed Res Int*. 2017;2017. doi:10.1155/2017/8584753,.

7. Motohashi O, Suzuki M, Shida N, Umezawa K, Ohtoh T, Sakurai Y, Yoshimoto T. Subarachnoid haemorrhage induced proliferation of leptomeningeal cells and

deposition of extracellular matrices in the arachnoid granulations and subarachnoid space - Immunhistochemical study. *Acta Neurochir (Wien)*. 1995;136:88–91.

8. Hewitt B, Ali M, Hubbard J, Hill L, Botfield H. A systematic review of the differential effects of TGFβ-1 in ischemic and hemorrhagic pre-clinical stroke models. *J Am Heart Assoc*. 2025.

9. LI CL, McILWAIN H. Maintenance of resting membrane potentials in slices of mammalian cerebral cortex and other tissues in vitro. *J Physiol*. 1957;139:178.

10. Croft CL, Futch HS, Moore BD, Golde TE. Organotypic brain slice cultures to model neurodegenerative proteinopathies. *Molecular neurodegeneration 2019 14:1*. 2019;14:1–11.

11. Eisemann T, Costa B, Strelau J, Mittelbronn M, Angel P, Peterziel H. An advanced glioma cell invasion assay based on organotypic brain slice cultures. *BMC Cancer*. 2018;18:1–10.

12. Magalhães DM, Pereira N, Rombo DM, Beltrão-Cavacas C, Sebastião AM, Valente CA. Ex vivo model of epilepsy in organotypic slices-a new tool for drug screening. *J Neuroinflammation*. 2018;15:1–18.

13. Humpel C. Organotypic brain slice cultures: A review. *Neuroscience*. 2015;305:86–98.

14. Alaylioğlu M, Dursun E, Yilmazer S, Gezen Ak D. A Bridge Between in vitro and in vivo Studies in Neuroscience: Organotypic Brain Slice Cultures. *Archives of neuropsychiatry*. 2020;57:333.

15. Jacobs BS, Boden-Albala B, Lin IF, Sacco RL. Stroke in the young in the Northern Manhattan stroke study. *Stroke*. 2002;33:2789–2793.

544 16. Mokrushin AA, Khama-Murad AX, Pavlinova LI. Effects of Long-Term Exposure of
545 Nerve Cells to Autoblood in In Vitro Model of Hemorrhagic Stroke. ; 2008: 1-355–
546 357.

547 17. Schindelin J, Arganda-Carreras I, Frise E, Kaynig V, Longair M, Pietzsch T, Preibisch
548 S, Rueden C, Saalfeld S, Schmid B, et al. Fiji: An open-source platform for biological-
549 image analysis. Nat Methods. . 2012;9:676–682.

550 18. Liao Y, Smyth GK, Shi W. featureCounts: an efficient general purpose program for
551 assigning sequence reads to genomic features. *Bioinformatics*. 2014;30:923–930.

552 19. Abueg LAL, Afgan E, Allart O, Awan AH, Bacon WA, Baker D, Bassetti M, Batut B,
553 Bernt M, Blankenberg D, et al. The Galaxy platform for accessible, reproducible, and
554 collaborative data analyses: 2024 update. *Nucleic Acids Res*. 2024;52:W83–W94.

555 20. Ewels P, Magnusson M, Lundin S, Käller M. MultiQC: summarize analysis results for
556 multiple tools and samples in a single report. *Bioinformatics*. 2016;32:3047–3048.

557 21. Love MI, Huber W, Anders S. Moderated estimation of fold change and dispersion for
558 RNA-seq data with DESeq2. *Genome Biol*. 2014;15:1–21.

559 22. Young MD, Wakefield MJ, Smyth GK, Oshlack A. Gene ontology analysis for RNA-
560 seq: accounting for selection bias. *Genome Biol*. 2010;11:1–12.

561 23. Pekny M, Pekna M. Astrocyte reactivity and reactive astrogliosis: Costs and benefits.
562 *Physiol Rev*. 2014;94:1077–1098.

563 24. Stence N, Waite M, Dailey ME. Dynamics of microglial activation: A confocal time-
564 lapse analysis in hippocampal slices. *Glia*. 2001;33:256–266.

565 25. Humpel C. Long-term live-cell imaging of GFAP+ astroglia and laminin+ vessels in
566 organotypic mouse brain slices using microcontact printing. *Front Cell Neurosci*.
567 2025;19:1540150.

568 26. Delbridge ARD, Huh D, Brickelmaier M, Burns JC, Roberts C, Challa R, Raymond N,
569 Cullen P, Carlile TM, Ennis KA, et al. Organotypic Brain Slice Culture Microglia
570 Exhibit Molecular Similarity to Acutely-Isolated Adult Microglia and Provide a
571 Platform to Study Neuroinflammation. *Front Cell Neurosci*. 2020;14:592005.

572 27. Li YSJ, Haga JH, Chien S. Molecular basis of the effects of shear stress on vascular
573 endothelial cells. *J Biomech*. 2005;38:1949–1971.

574 28. Vyalov S, Langille BL, Gotlieb AI. Decreased blood flow rate disrupts endothelial
575 repair in vivo. *Am J Pathol*. 1996;149:2107.

576 29. Sho E, Sho M, Singh TM, Xu C, Zarins CK, Masuda H. Blood flow decrease induces
577 apoptosis of endothelial cells in previously dilated arteries resulting from chronic high
578 blood flow. *Arterioscler Thromb Vasc Biol*. 2001;21:1139–1145.

579 30. Moser K V., Schmidt-Kastner R, Hinterhuber H, Humpel C. Brain capillaries and
580 cholinergic neurons persist in organotypic brain slices in the absence of blood flow.
581 *European journal of neuroscience*. 2003;18:85–94.

582 31. Ward MR, Tsao PS, Agrotis A, Dilley RJ, Jennings GL, Bobik A. Low blood flow after
583 angioplasty augments mechanisms of restenosis: inward vessel remodeling, cell
584 migration, and activity of genes regulating migration. *Arterioscler Thromb Vasc Biol*.
585 2001;21:208–213.

586 32. Ueno H, Kanellakis P, Agrotis A, Bobik A. Blood flow regulates the development of
587 vascular hypertrophy, smooth muscle cell proliferation, and endothelial cell nitric
588 oxide synthase in hypertension. *Hypertension*. 2000;36:89–96.

589 33. Andrews RN, Caudell DL, Metheny-Barlow LJ, Peiffer AM, Tooze JA, Bourland JD,
590 Hampson RE, Deadwyler SA, Cline JM. Fibronectin Produced by Cerebral Endothelial
591 and Vascular Smooth Muscle Cells Contributes to Perivascular Extracellular Matrix in
592 Late-Delayed Radiation-Induced Brain Injury. *Radiat Res*. 2018;190:361–373.

593 34. Altrock E, Sens C, Wuerfel C, Vasel M, Kawelke N, Dooley S, Sottile J, Nakchbandi
594 IA. Inhibition of fibronectin deposition improves experimental liver fibrosis. *J*
595 *Hepatol*. 2015;62:625–633.

596 35. Stichel CC, Hermanns S, Luhmann HJ, Lausberg F, Niermann H, D'Urso D, Servos G,
597 Hartwig H-G, Müller HW. Inhibition of collagen IV deposition promotes regeneration
598 of injured CNS axons. *European journal of neuroscience*. 1999;11:632–646.

599 36. Klapka N, Hermanns S, Straten G, Masanneck C, Duis S, Hamers FPT, Müller D,
600 Zuschratter W, Müller HW. Suppression of fibrous scarring in spinal cord injury of rat
601 promotes long-distance regeneration of corticospinal tract axons, rescue of primary
602 motoneurons in somatosensory cortex and significant functional recovery. *Eur J*
603 *Neurosci*. 2005;22:3047–3058.

604 37. Li H, Ghorbani S, Ling CC, Yong VW, Xue M. The extracellular matrix as modifier of
605 neuroinflammation and recovery in ischemic stroke and intracerebral hemorrhage.
606 *Neurobiol Dis*. 2023;186. doi:10.1016/j.nbd.2023.106282.

607 38. Li H, Ghorbani S, Zhang R, Ebacher V, Stephenson EL, Keough MB, Yong VW, Xue
608 M. Prominent elevation of extracellular matrix molecules in intracerebral hemorrhage.
609 *Front Mol Neurosci*. 2023;16:1251432.

610 39. Macdonald RL, Weir BKA, Young JD, Grace MGA. Cytoskeletal and extracellular
611 matrix proteins in cerebral arteries following subarachnoid hemorrhage in monkeys. *J*
612 *Neurosurg*. 1992;76:81–90.

613 40. Howe M. The Role Of Perivascular Fibrosis In Post-Stroke Glymphatic Impairment
614 And Cerebral Amyloid Angiopathy. *Dissertations & theses (open access)*. 2018.
615 Available at https://digitalcommons.library.tmc.edu/utgsbs_dissertations/875. Accessed
616 February 28, 2025.

617 41. Das M, Leonardo CC, Rangooni S, Mohapatra SS, Mohapatra S, Pennypacker KR.
618 Lateral fluid percussion injury of the brain induces CCL20 inflammatory chemokine
619 expression in rats. *J Neuroinflammation*. 2011;8:1–16.

620 42. Liao LS, Zhang MW, Gu YJ, Sun XC. Targeting CCL20 inhibits subarachnoid
621 hemorrhage-related neuroinflammation in mice. *Aging*. 2020;12:14849–14862.

622 43. Fang HY, Ko WJ, Lin CY. Plasma interleukin 11 levels correlate with outcome of
623 spontaneous intracerebral hemorrhage. *Surg Neurol*. 2005;64:511–517.

624 44. Seyedsadr M, Wang Y, Elzoheiry M, Gopal SS, Jang S, Duran G, Chervoneva I,
625 Kasimoglou E, Wrobel JA, Hwang D, et al. IL-11 induces NLRP3 inflammasome
626 activation in monocytes and inflammatory cell migration to the central nervous system.
627 *Proc Natl Acad Sci U S A*. 2023;120:e2221007120.

628 45. Zhang B, Zhang HX, Shi ST, Bai YL, Zhe X, Zhang SJ, Li YJ. Interleukin-11
629 treatment protected against cerebral ischemia/reperfusion injury. *Biomedicine &*
630 *pharmacotherapy*. 2019;115:108816.

631 46. Garcia-Bonilla L, Racchumi G, Murphy M, Anrather J, Iadecola C. Endothelial CD36
632 Contributes to Postischemic Brain Injury by Promoting Neutrophil Activation via
633 CSF3. *Journal of neuroscience*. 2015;35:14783–14793.

634 47. Madangarli N, Bonsack F, Dasari R, Sukumari–Ramesh S. Intracerebral Hemorrhage:
635 Blood Components and Neurotoxicity. *Brain Sci*. 2019;9:316.

636 48. Alsbrook DL, Di Napoli M, Bhatia K, Biller J, Andalib S, Hinduja A, Rodrigues R,
637 Rodriguez M, Sabbagh SY, Selim M, et al. Neuroinflammation in Acute Ischemic and
638 Hemorrhagic Stroke. *Curr Neurol Neurosci Rep*. 2023;23:407–431.

639 49. Zhou P, Yang C, Zhang S, Ke ZX, Chen DX, Li YQ, Li Q. The Imbalance of MMP-
640 2/TIMP-2 and MMP-9/TIMP-1 Contributes to Collagen Deposition Disorder in
641 Diabetic Non-Injured Skin. *Front Endocrinol (Lausanne)*. 2021;12:734485.

642 50. Chen G, Ge D, Zhu B, Shi H, Ma Q. Upregulation of matrix metalloproteinase 9
643 (MMP9)/tissue inhibitor of metalloproteinase 1 (TIMP1) and MMP2/TIMP2 ratios
644 may be involved in lipopolysaccharide-induced acute lung injury. *J Int Med Res*.
645 2020;48:0300060520919592.

646 51. Solár P, Zamani A, Lakatosová K, Joukal M. The blood–brain barrier and the
647 neurovascular unit in subarachnoid hemorrhage: molecular events and potential
648 treatments. *Fluids and barriers of the cns 2022 19:1*. 2022;19:1–79.

649

650 **9. <u>Tables</u>**

651

652 **Table 1 – Antibody dilutions used in immunofluorescent staining of OBSCs.**

Antibody	Dilution
Anti-rat endothelial cell antigen 1 (RECA-1), mouse	1:100
Anti-fibronectin, rabbit	1:400
Anti-alpha smooth muscle actin (αSMA), mouse	1:500
Anti-cleaved caspase 3 (CCP3), rabbit	1:500
Anti-NeuN, mouse	1:500
Anti-GFAP, mouse	1:400
Anti-collagen IV, rabbit	1:500
Anti-IBA1, rabbit	1:500
AF488 conjugated anti-rabbit IgG, highly cross-absorbed	1:1000
AF594 conjugated anti-mouse IgG, highly cross-absorbed	1:1000

653

654

655 **Table 2 - Table showing reagent, source and catalogue number / identifier for all key**
656 **resources used in the present work.**

REAGENT or RESOURCE	SOURCE	IDENTIFIER
Antibodies		
Anti-rat endothelial cell antigen 1 (RECA-1), mouse	Abcam	CAT# Ab9774
Anti-fibronectin, rabbit	Invitrogen	CAT# F3648
Anti-alpha smooth muscle actin (αSMA), mouse	ThermoFisher	CAT# 14-9760-82
Anti-cleaved caspase 3 (CCP3), rabbit	Cell Signalling Technologies	CAT# CST96615
Anti-NeuN, mouse	Cell Signalling Technologies	CAT# 94403
Anti-GFAP, mouse	Sigma	CAT# G3893
Anti-collagen IV, rabbit	BioRad	CAT# 2150-1470
Anti-IBA1, rabbit	FujiFilm Wako	CAT# 019-19741

AF488 conjugated anti-rabbit IgG, highly cross-absorbed	ThermoFisher	CAT# A32731
AF594 conjugated anti-mouse IgG, highly cross-absorbed	ThermoFisher	CAT# A32742
Anti-alpha-actin	Abcam	CAT# Ab179467
Anti-IgG HRP conjugated	Abcam	CAT# Ab6721
Chemicals, Peptides and Recombinant Proteins		
Earle's balanced salt solution	Gibco	CAT# 11540616
HEPES	Fisher Scientific	CAT# 10204932
DMEM cell culture medium	Fisher Scientific	CAT# 11965092
Neurobasal A	Fisher Scientific	CAT# 11540366
B-27	Fisher Scientific	CAT# 11530536
L-glutamine	ThermoFisher	CAT# 25030024
Penicillin-Streptomycin	ThermoFisher	CAT# 15070063
Pentoject, Pentobarbital sodium	Animalcare	CAT# XVD132
Cyanoacrylate glue	RS	CAT# 835-4131
Paraformaldehyde	Merck	CAT# 47608-1L-F
Phosphate Buffered Saline (PBS) tablets	Fisher Scientific	CAT# 10209252
Triton X-100	Merck	CAT#X100-1GA
Goat serum	Fisher Scientific	CAT# 11530526
4′,6-diamidino-2-phenylindole (DAPI)	Invitrogen	CAT# D21490
Radioimmunoprecipitation assay (RIPA) buffer	ThermoFisher	CAT# 89900
cOmplete™ Protease Inhibitor Cocktail	Roche	CAT# 11697498001
PhosSTOP™ Phosphatase Inhibitor	Roche	CAT# 4906845001
Lithium Dodecyl Sulfate (LDS) buffer	ThermoFisher	CAT# NP0007
Sample Reducing Agent	ThermoFisher	CAT# NP0004
Bis-Tris Mini Protein Gels, 4–12%	ThermoFisher	CAT# NP0322
MOPS SDS Running Buffer	ThermoFisher	CAT# NP0001
Protran 0.45 NC nitrocellulose Western blotting membranes	Cytiva	CAT# 10600007
NuPAGE™ Transfer Buffer	ThermoFisher	CAT# NP00061
Skimmed milk powder	VWR	CAT#84615.0500
Tris-buffered saline	Merck	CAT#524750

Tween20	Scientific Laboratory Supplies	CAT#CHE3852
SuperSignal™ West Pico PLUS Chemiluminescent Substrate	ThermoFisher	CAT# 34580
TRIzol	Invitrogen	CAT# 12044977
Chloroform	ThermoFisher	CAT# J67241.K2
Molecular grade ethanol	Fisher Scientific	CAT#BP2818-212
RNase-Free Water	Qiagen	CAT# 129112
Nuclease-Free Water	Qiagen	CAT# 129117
SYBR™ Green Universal Master Mix	ThermoFisher	CAT# 43-091-55
Critical Commercial Assays		
Bicinchoninic Acid (BCA) Assay Kit	ThermoFisher	CAT# 23225
RNeasy Mini Kit	Qiagen	CAT# 74104
Tetro™ cDNA Synthesis Kit	Bioline	CAT# BIO65043
Experimental Models: Organisms/Strains		
Sprague-Dawley rat	Inotiv	CAT# 002
Oligonucleotides		
Primers for quantitative reverse-transcription PCR (RT-qPCR)	Supplemental materials Table S2	Supplemental materials Table S2
Software and Algorithms		
FIJI	FIJI	https://fiji.sc/
Image processing macro: Percentage coverage of blood vessels	This paper	https://github.com/Dr-ben-hewitt/OBSC-quantification-macros
Image processing macro: Intensity per unit area	This paper	https://github.com/Dr-ben-hewitt/OBSC-quantification-macros
Galaxy	Galaxy	https://usegalaxy.org/
GraphPad Prism 10.3	Graphpad	https://www.graphpad.com/scientific-software/prism
QBase+	CellCarta	https://cellcarta.com/genomic-data-analysis/
Zen 3.1	Zeiss	https://www.zeiss.com/microscopy/en/products/software/zeiss-zen.html
GeneSys / GeneTools	SynGene	https://www.syngene.com/software/

659 **10. Figures**

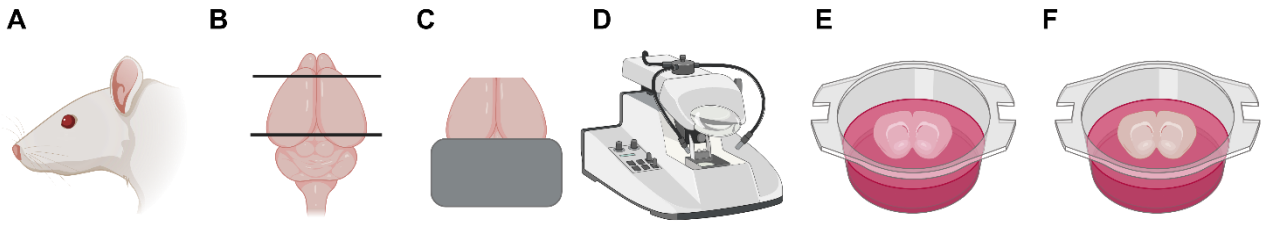

660

661 **Figure 1 – Steps in the generation of adult rat brain OBSCs.** A) Sacrifice and brain
662 removal, B) Removal of olfactory bulbs and cerebellum, including production of a flat edge
663 on the caudal aspect of the cerebrum, C) Mounting of brain (caudal face down) onto
664 vibratome chuck with cyanoacrylate glue, D) Vibratome slicing of brain (250 µM sections, 80
665 Hz, 1.25 mm amplitude), E) Brain slices added to 6-well cell culture inserts, F) Media
666 removed to bring brain slice to air-liquid interface.

667

668

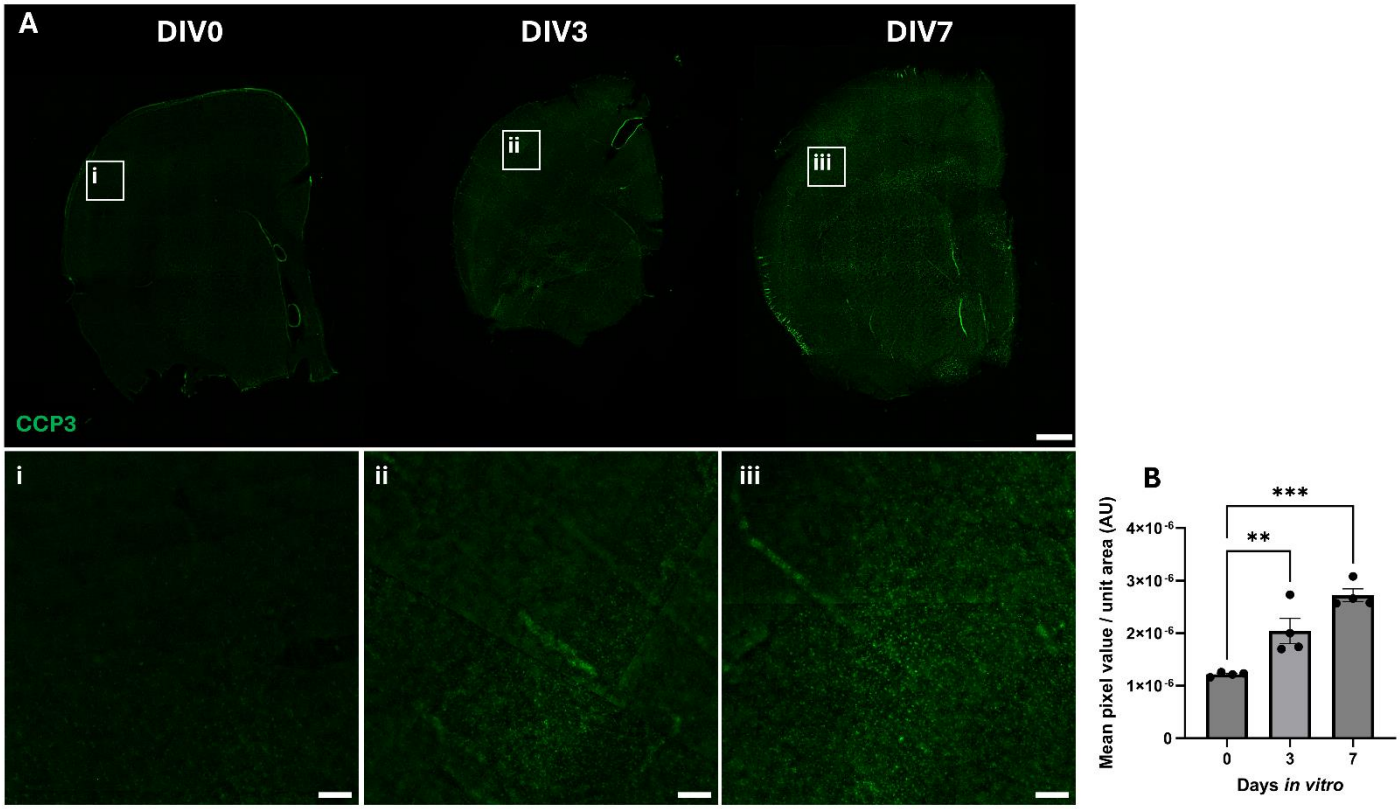

669 **Figure 2 – Distribution and intensity of CCP3 throughout control and cultured OBSCs.**
670 A) Representative immunofluorescent staining of OBSCs (CCP3, green and DAPI, blue) at 0
671 3 and 7 days *in vitro* (scale bar = 1,000 µm). Magnified regions of the cortex of section are
672 shown in insets 'i', 'ii' and 'iii' for DIV0, 3 and 7 respectively (scale bar = 100 µm for all).

Quantification of mean CCP3-stained pixel intensity per unit area in the cortex was also performed (B). Each image quantification datapoint is mean of 6 regions of interest from 2 brain slices per animal (3 regions per slice), ± SEM. One-way ANOVA with Dunnett's multiple comparisons test (all to all). ns = not significant, ** $P < 0.01$, *** $P < 0.001$. $N = 4$ animals, $\alpha = 0.05$.

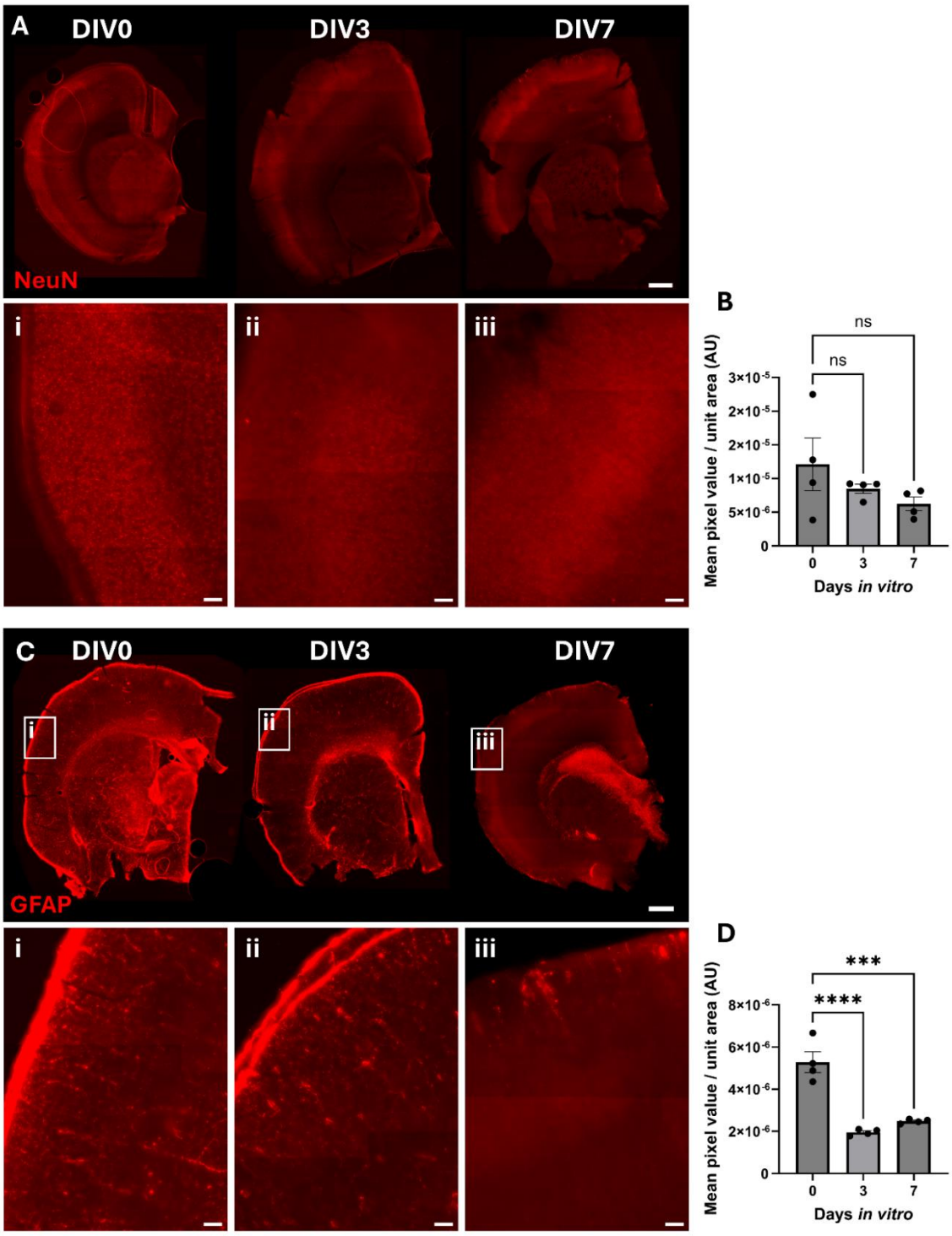

Figure 3 - Immunofluorescent staining of neurons and astrocytes in OBSCs after 0, 3 and 7 days *in* vitro (DIV). Representative immunofluorescent staining of A) NeuN (neuronal cell marker) and C) GFAP (astrocyte marker) shown in red, with DAPI nuclear counterstain in blue (scale bars = 1,000 µm). Magnified regions of the cortex of section are shown in insets 'i', 'ii' and 'iii' for DIV0, 3 and 7 respectively (scale bars = 100 µm in insets), in addition to quantification of the mean pixel value per unit area for these regions in insets B) NeuN quantification in cortex, D) GFAP quantification in cortex. Each datapoint is the mean of 3 regions of interest per brain slice, ±SEM. All statistics were performed with

one-way ANOVA with Dunnett's multiple comparisons test (all to control). ns = not significant, ** $P < 0.01$, *** $P < 0.001$, **** $P < 0.0001$. $N = 4$ animals, $\alpha = 0.05$.

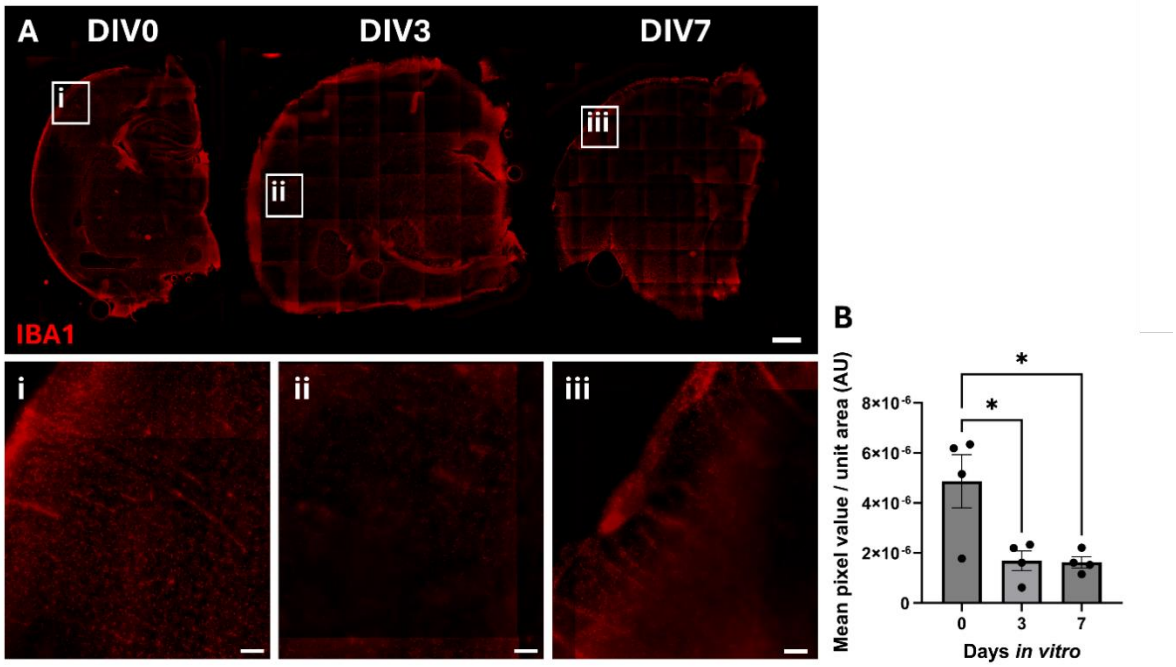

Figure 4 - Immunofluorescent staining of microglia in OBSCs after 0, 3 and 7 days *in vitro* (DIV). Representative immunofluorescent staining of IBA1 shown in red (scale bars = 1000 µm). Magnified regions of the cortex of section are shown in insets 'i', 'ii' and 'iii' for DIV0, 3 and 7 respectively, in addition to quantification of the mean pixel value per unit area (scale bars = 100 µm in insets). Each datapoint is the mean of 3 regions of interest per brain slice, ±SEM. All statistics were performed with one-way ANOVA with Dunnett's multiple comparisons test (all to control). ns = not significant, * $P < 0.05$. $N = 4$ animals, $\alpha = 0.05$.

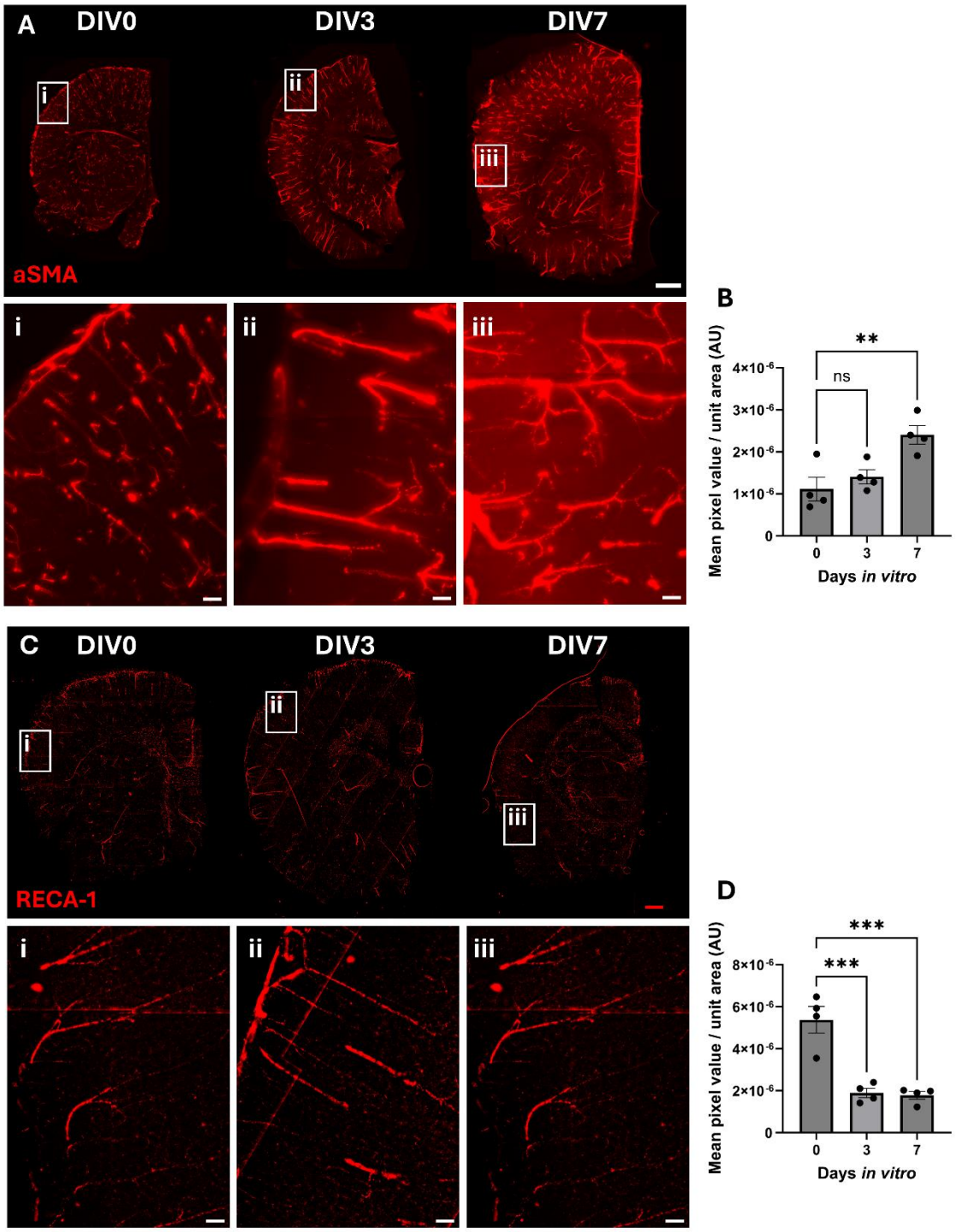

Figure 5 - Immunofluorescent staining of smooth muscle cells, pericytes and endothelial cells in OBSCs after 0, 3 and 7 days *in* vitro (DIV). Representative immunofluorescent staining of A) αSMA (alpha smooth muscle actin) and C) rat endothelial cell antigen 1 (RECA-1) shown in red (scale bars = 1,000 µm). Magnified regions of the cortex of section are shown in insets 'i', 'ii' and 'iii' for DIV0, 3 and 7 respectively (scale bars = 100 µm in insets), in addition to quantification of the mean pixel value per unit area for these regions B) αSMA quantification, D) RECA1 quantification. Each datapoint is mean of 3 regions of interest per brain slice, ±SEM. All statistics were performed with one-way ANOVA with Dunnett's multiple comparisons test (all to control). ns = not significant, ** $P < 0.01$, *** $P < 0.001$, **** $P < 0.0001$. $N = 4$ animals, $\alpha = 0.05$.

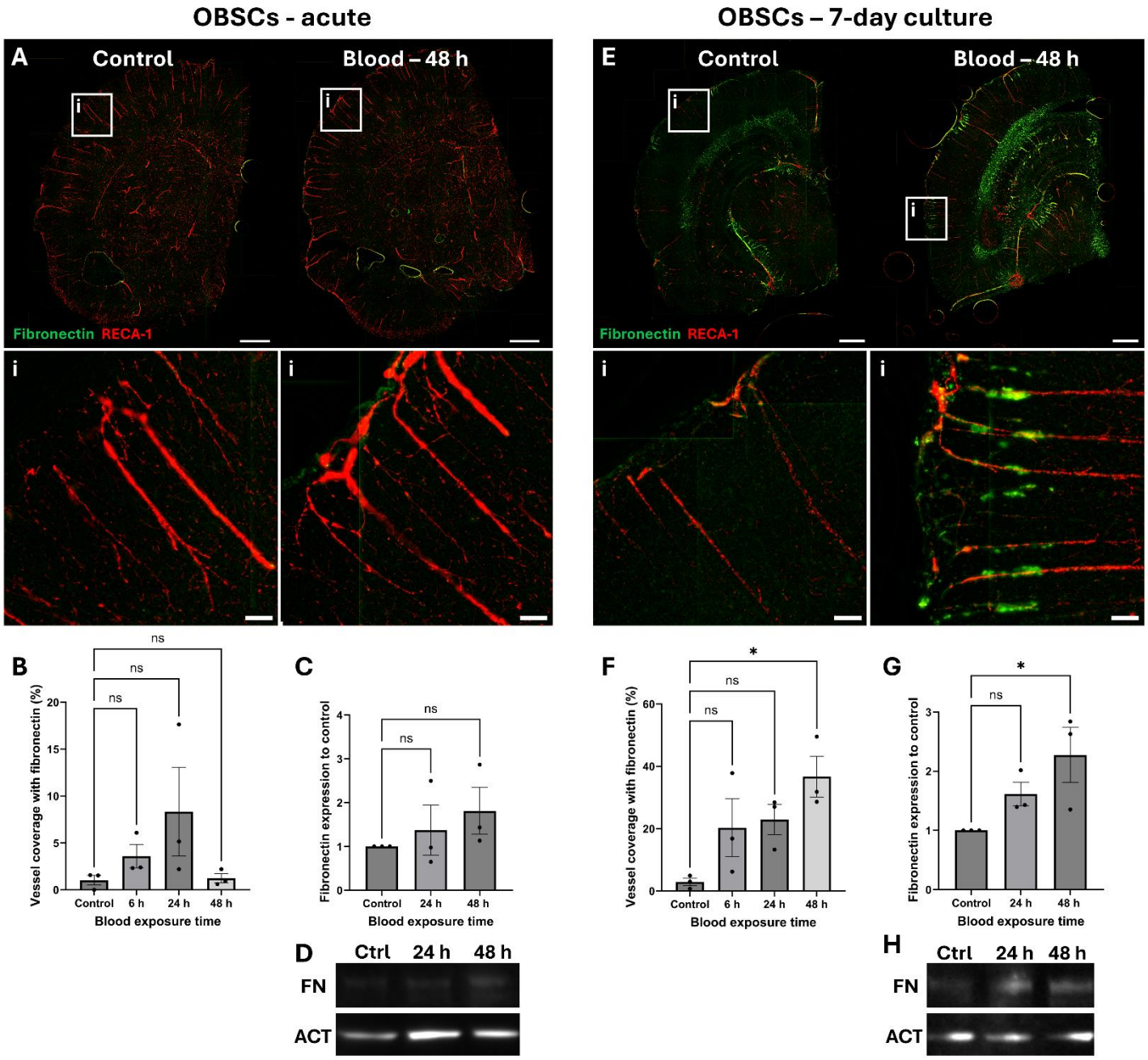

Figure 6 – Localisation and quantification of fibronectin in blood-exposed OBSCs. OBSCs were generated and cultured either for 0 or 7 days, after which they were exposed either to PBS (control) or the same volume of lysed blood for 48 hours. OBSCs were then fixed and stained for RECA1 (red) and fibronectin (green). Representative images of whole hemispheres are shown (A – acute, E – 7 day pre-cultured, scale bars = 1,000 µm). Insets show magnified regions of the cortex (i) (scale bars = 100 µm). Quantification of the percentage coverage of fibronectin on RECA1-stained vessels was performed (B, F). Fibronectin protein expression at 24 and 48 hours of blood exposure was also assessed by Western blot (D, H), followed by quantification of fibronectin fold-change (C, G). Each image quantification datapoint is the mean of three regions of interest from one brain slice per animal, ± SEM. All statistics were performed with one-way ANOVA with Dunnett's multiple comparisons test (all to control). ns = not significant, $N = 3$ animals, $\alpha = 0.05$.

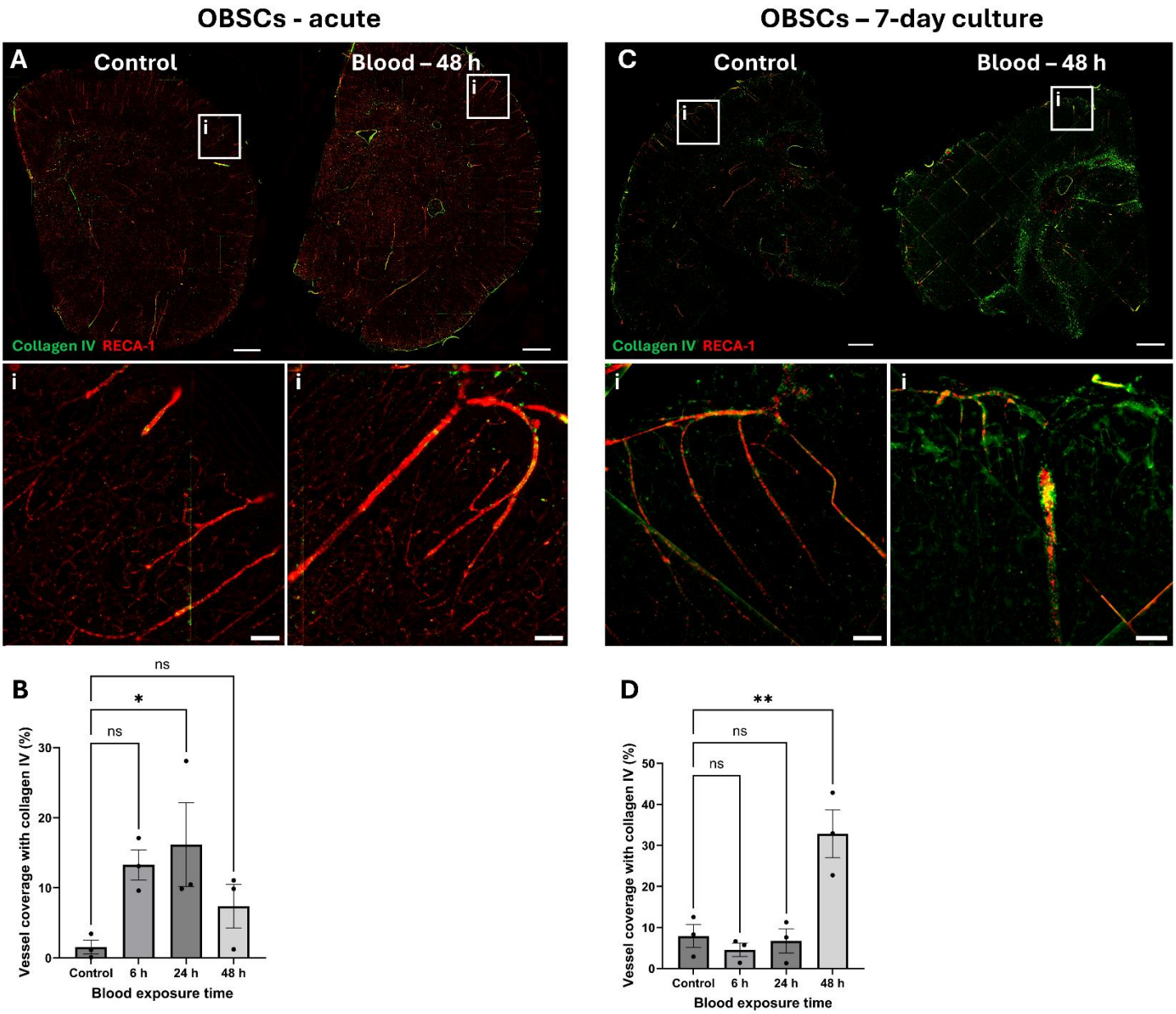

Figure 7 - Localisation and quantification of collagen IV in blood-exposed OBSCs. OBSCs were generated and cultured either for 0 or 7 days, after which they were exposed either to PBS (control) or the same volume of lysed blood for 48 hours. OBSCs were then fixed and stained for RECA1 (red) and collagen IV (green). Representative images of whole hemispheres are shown (A – acute, C – 7 day pre-cultured, scale bars = 1,000 µm). Insets show magnified regions of the cortex (i) (scale bars = 100 µm). Quantification of the percentage coverage of collagen IV on RECA1-stained vessels was performed (B, D). Each image quantification datapoint is the mean of three regions of interest from one brain slice per animal, ± SEM. All statistics were performed with one-way ANOVA with Dunnett's multiple comparisons test (all to control). ns = not significant, $N = 3$ animals, $\alpha = 0.05$.

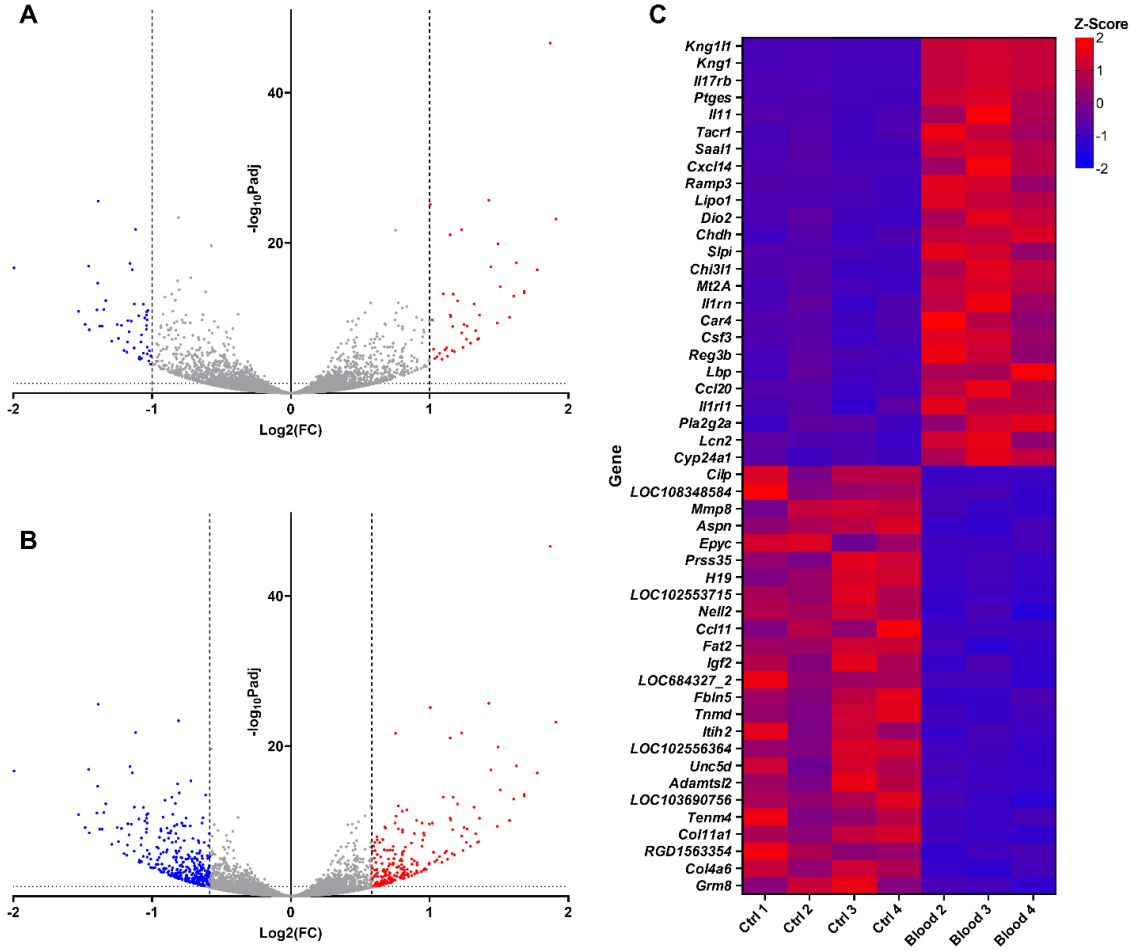

Figure 8 - Volcano plots and heatmap of top 25 most differentially expressed genes (DEGs) in control and blood-treated OBSCs. Volcano plots set with a fold change threshold >2 (A) and >1.5 (B) (with fold change thresholds depicted by dotted vertical lines), showing upregulated DEGs (*pAdj* < 0.05) in red and downregulated DEGs in blue. Z-scores for top 25 most up- and down-regulated DEGs (ranked by $\log_2$ fold change) are visualised via heatmap (C), with upregulated genes shown in red and downregulated genes in blue.

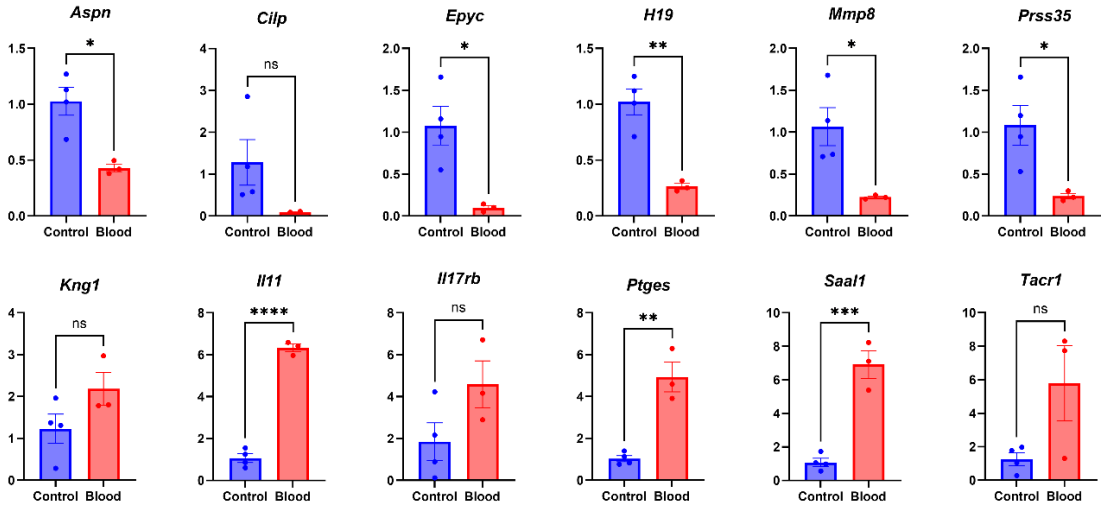

Figure 9 - RT-qPCR validation of RNA-sequencing. Top 6 downregulated (lower expression in blood-exposed samples) and top 6 upregulated (higher expression in blood-exposed samples). All statistical analyses were performed with unpaired t-tests. ns = not significant, ns = not significant, * $P < 0.05$, ** $P < 0.01$, *** $P < 0.001$, **** $P < 0.0001$, $N = 3$, $\alpha = 0.05$.

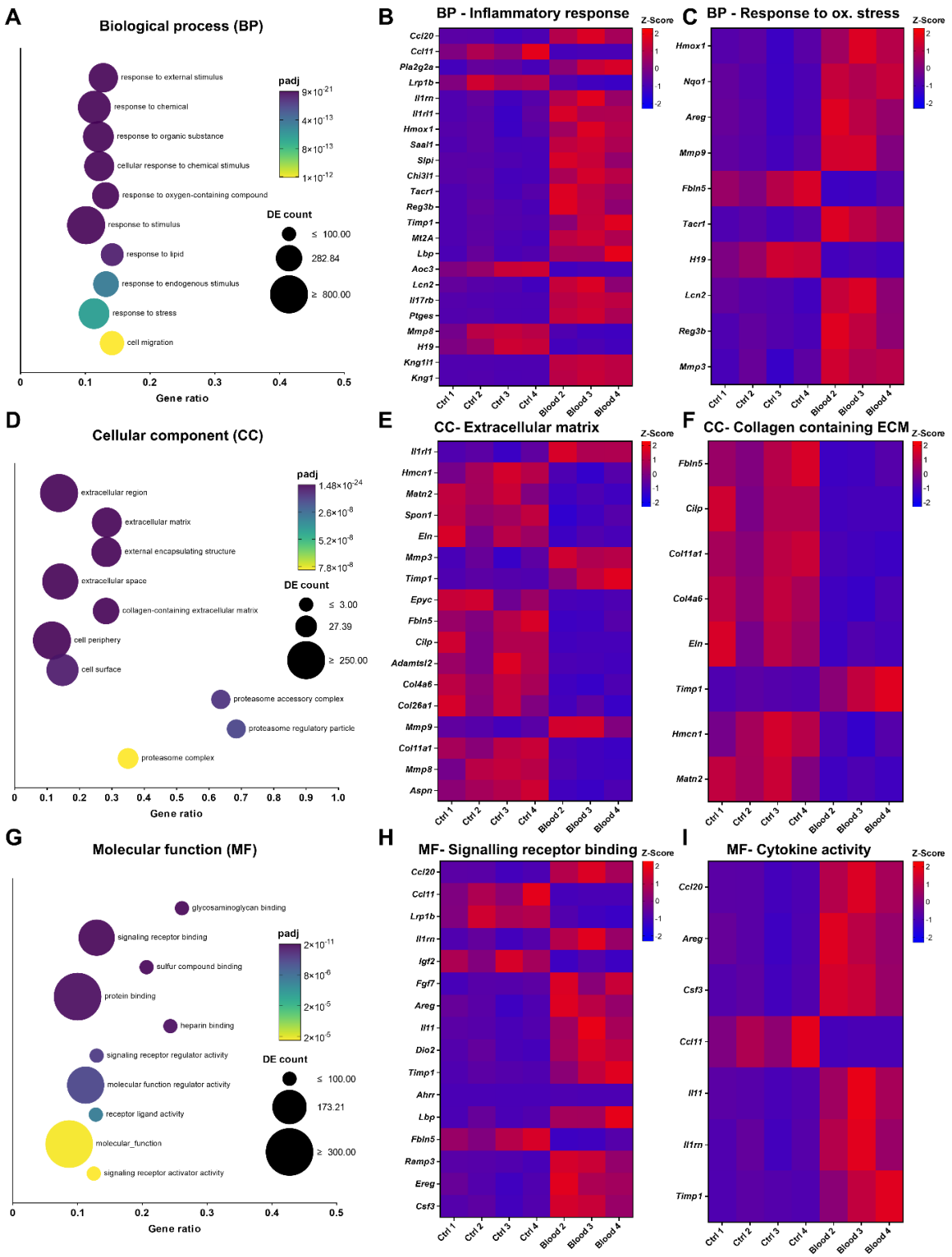

Figure 10 – Gene ontology (GO) for control and blood-treated OBSC, with DEGs from selected GO terms within each family. A, D, G) Biological process, cellular component and molecular function GO families depicted with the top 10 most significant overrepresented CC GO terms shown as a bubble plot. The colour scale depicts adjusted p-value (*padj*) and bubble size represents the number of differentially expressed genes included in the respective category. Gene ratio of 1 = all genes in the GO category are DE, whilst 0 = none. B, C, E, F,

H, I) Heatmaps of Z-score of DEGs with FC>2 or <0.5 within selected significantly over-represented GO terms ‘inflammatory response’, ‘response to oxidative stress’, ‘extracellular matrix’, ‘collagen containing extracellular matrix’, ‘signalling receptor binding’ and ‘cytokine activity’ respectively.